Effects of lateral boundaries on traveling-wave dynamics in binary fluid convection

C. M. Aegerter and C. M. Surko

Department of Physics 0319, University of California San Diego, La Jolla, California 92093

The global dynamics of traveling-wave patterns in convection in a mixture of ethanol in water is studied in different cell geometries: circular, rectangular, and stadium-shaped cells. The dynamics in these cells differ greatly, changing from a globally rotating state in the circular cell, to one large domain of locally parallel traveling waves in the rectangular cell, to a continually chaotic state in the stadium cell. In all three cases, the patterns can be described in terms of the phase of the complex order parameter. Disorder in the patterns is quantified in terms of topological defects in the phase field. While the numbers, net charge, and dynamics of defects differ greatly in the patterns in the three cells, the local dynamics of the defects, as measured by the defect-defect correlation functions, are similar.

I. INTRODUCTION

When a physical system is driven out of thermodynamic equilibrium, it generally undergoes symmetry breaking transitions leading to the formation of a variety of patterns [1]. Depending on the detailed nature of the system, the patterns at onset may be stationary or show an intrinsic time dependence. In this paper we study the dynamics of patterns in the special case of convection in a binary fluid mixture in which the patterns at onset consist of traveling waves [2]. It is important to emphasize, however, that such studies may also address problems in seemingly unrelated nonequilibrium systems that exhibit oscillatory instabilities. Thus, the studies described here are potentially relevant in such diverse fields as nonlinear optics in large aspect ratio lasers [3]; population dynamics in ecology [4] and epidemiology [5]; electric signaling in the heart [6]; chemical waves in reaction-diffusion systems [7,8]; the magnetic dynamo in the solar plasma [9]; self-organization in colonies of amoebas [10,11]; and, in some instances, the dynamics of driven magnetic flux vortices in superconductors [12,13]. Study of patterns and dynamics in convecting fluids has a number of potential advantages when the goal is to elucidate the fundamental physical principles underlying the patterns and dynamics in nonequilibrium systems. Convection in pure fluids can be described by two dimensionless parameters, the Rayleigh and Prantl numbers, defined by [14]

$$\mathrm{Ra} = \frac{g\,\alpha h^3 \Delta T}{\nu \kappa}, \qquad (1)$$

$$\mathrm{Pr} = \frac{\nu}{\kappa}, \qquad (2)$$

where α is the thermal expansion coefficient, ν is the kinematic viscosity, κ is the thermal diffusivity, h is the height of the fluid layer, ΔT is the imposed temperature difference, and g is the acceleration due to gravity. From an experimental viewpoint, excellent control of the system can be achieved, providing a high degree of repeatability in experiments. On the theoretical side, models of fluid dynamics are developed to a high level of sophistication. The Navier-Stokes equation provides an exact description on which approximate models can be based. As a consequence, many fundamental questions in pattern formation have been first addressed in the framework of convection and then subsequently applied to other situations, such as those of technological relevance.

The influence of boundary conditions on patterns in convection has been studied extensively. Mostly these studies have concentrated on the investigation of convection in pure fluids, in which the patterns are stationary. When the initial instability is to a stationary pattern, the nature of the boundary is very important. In the case of classical Rayleigh-Bénard convection, rolls of convection form the stable pattern, whereas with different boundary conditions imposed on the top plate (e.g., corresponding to an open container) hexagonal patterns are observed [14]. Similarly, the thermal conductivity of the boundary can play an important role, as has been discussed by Clever and Busse [15], who calculated the stability balloon for convection with one boundary nearly thermally insulating. They predict that in such a case a pattern intermediate between rolls and hexagons (''hexarolls'') is stable. Typically, the presence of a lateral boundary induces finite size effects, which result, for instance, in a small change in the critical Rayleigh number [16]. However, in the case where there is an additional breaking of left-right symmetry of the convection rolls (e.g., by imposing a global, unidirectional flow in the convecting fluid), lateral boundaries can also be instrumental in determining the pattern selection [17].

In the case where the initial instability is oscillatory, and the patterns at onset consist of traveling waves, theoretical investigations of the effects of distant boundaries have shown that their presence can substantially alter the nature of the instability, even in one dimension [18,19]. For example, changes in boundary conditions can change not only the critical value of the control parameter but also the frequency of the traveling waves at onset. In the work presented here, we report experimental studies of the dynamics of two-dimensional convection patterns in a binary fluid mixture of ethanol and water in cells of different shapes. For the regime of parameters studied, convection begins with a subcritical bifurcation to states of traveling waves. In the two-

dimensional patterns studied here, not only does the presence of the lateral boundaries alter the dynamics of the patterns significantly, but their shape does also. This is likely due to the fact that different regions of the boundary can have different, competing effects at a single point within the cell. The curvature of the lateral boundaries may also play an important role in the dynamics. The cell shapes studied here correspond to different extremes. In the rectangular cell, the curvature of the boundary is zero almost everywhere, apart from very small regions at the corners of the cell, where it is very large. In the stadium-shaped cell, segments of zero curvature are separated by approximately equal lengths with a constant, nonzero curvature. Finally, in the circular cell the curvature is constant and nonzero along the entire boundary. As we describe below, this leads to vastly different global dynamics of the patterns in the three cases.

Previous investigations of traveling-wave convection in a circular cell have shown that the patterns evolve to a state in which the entire pattern rotates [20–22]. In the course of this self-organization, the pattern evolves to a small number (e.g., four or five) domains of locally parallel traveling waves. These domains share sources and sinks of the waves pairwise along the boundary, such that the source of one acts as the sink of another, giving the impression of a global rotation of the pattern. This symmetry between sources and sinks of traveling waves along the boundary may reflect the symmetry of different points within the cell stemming from the circular boundary.

We find that this situation is qualitatively different when the geometry of the cell boundary is changed. In a rectangular cell, sources of traveling waves are almost always located at one of the corners of the cell. This is likely due to the fact that the curvature of the boundary is very large at the corners. At lower Rayleigh numbers, close to the saddle node, the dominant source becomes unstable, which leads to the creation of a dominant source in another corner. In the proximity of a corner, inhomogeneous flows or mixing may occur, which affect the effective local Rayleigh number. Close to the saddle node such a change will lead to a significant alteration of the frequency of the traveling waves [23]. This can in turn lead to the switching of domains observed. At higher Rayleigh numbers, a source in a corner is stable and dominates the entire pattern. This leads to very well ordered patterns consisting of a single domain with a relatively constant and uniform wave number and frequency.

In a stadium-shaped cell, the pattern dynamics are more chaotic. Globally rotating patterns can be produced in these cells; however, they are typically unstable. Moreover, the occurrence of a global rotation of the patterns depends on the way in which convection is initiated. In contrast to the circular cell, isolated sources do exist on the boundary of the stadium cell, similar to those in the rectangular cell. Due to the relatively small curvature of the boundary, however, these sources can move along the boundary. This movement appears to prevent the establishment of a single, dominant domain, in contrast to the patterns observed in the rectangular cell. The radius of curvature of the boundary, however, does not appear to be critical in determining the overall dynamics. In experiments in a circular cell with a radius of curvature equal to that of the stadium-shaped cell, global rotation of the pattern is observed to be stable, indicating the importance of the symmetry of the boundary in determining the dynamics.

Previous experiments in a large circular cell led to the development of a description of the traveling-wave patterns in terms of topological defects in the phase field of the order parameter [21,22]. When describing a pattern-forming system that exhibits an oscillatory instability, it is customary to introduce a complex order parameter [1,25]. It is then possible to demodulate the amplitude and the phase of this order parameter (see Sec. III below and Refs. [20,24]). In the case of traveling-wave convection in the mixtures studied here, the amplitude of convection is constant over most of the pattern, and thus the details of the pattern are contained in the phase of the order parameter. Since the distribution of wave numbers and frequencies was found to be very uniform within different traveling-wave domains, most of the information concerning the pattern is in the regions near the domain boundaries, which typically consist of lines of topological defects in the phase field [21]. As a consequence, the locking of different domains into states of global rotation in the circular cell is accompanied by a saturation of the net topological charge of the phase field at a value corresponding to the number of roll pairs along the boundary. The interactions between the defects, as evidenced by their mutual correlations, appears as if it could be a useful framework within which to understand this self-organization [22]. In the case of the rectangular and stadium-shaped cells investigated here, some of these features remain, while others clearly must be elaborated, as indicated by the different global dynamics that is observed. These issues will be discussed in detail below.

This paper is organized in the following way. In Sec. II, we describe convection in a binary fluid mixture. We concentrate on the traveling-wave regime of relevance here in which the Soret effect plays a crucial role. In Sec. III, we describe the experiment and data analysis procedures used. In Sec. IV we present and discuss the experimental results, and in Sec. V we offer a set of concluding remarks.

II. BINARY FLUID CONVECTION

Convection in mixtures can be qualitatively different from that in pure fluids, particularly near onset. The mixture adds a second diffusive quantity, the concentration, to the system besides temperature. Of particular relevance here is the coupling of these two quantities via the Soret effect [26,27], which is particularly strong in ethanol-water mixtures. Formally this leads to an additional term in the concentration current, which depends on the temperature gradient:

$$\mathbf{j}_c = -D_c \nabla c + D_c S_t c (1-c) \nabla T + \mathbf{u} c, \tag{3}$$

where $\mathbf{j}_c$ is the concentration flux, $\mathbf{u}$ is the fluid velocity, D_c is the concentration diffusivity and S_t is the Soret coefficient [26,27]. Due to the influence of the concentration on the density of the fluid and hence the buoyancy, there is a feedback of the temperature gradient on the fluid flow. As mentioned above, for the mixture studied here, the sign of S_t is
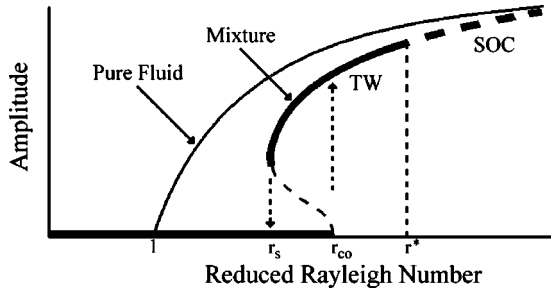
FIG. 1. Bifurcation diagram for binary fluid convection with a negative separation ratio for $\psi < -|\mathcal{L}|$. Due to the coupling of the concentration flux to the temperature gradient (via the Soret effect), the bifurcation is changed from supercritical, as in a pure fluid (thin line), to subcritical (see the text). Convection begins at a reduced Rayleigh number r_{co}, when the temperature difference is increased, and disappears at a saddle node at r_s when the Rayleigh number is decreased. The patterns become stationary at Rayleigh number r^*. SOC indicates stationary overturning convection and TW traveling wave.

such that the onset of convection occurs as a subcritical Hopf bifurcation. In this case, the linearly unstable state at onset has a frequency very different from that of the stable convecting state to which it evolves. The bifurcation diagram is illustrated in Fig. 1, where the Rayleigh number is given in terms of the critical value for onset in a pure fluid, which is the notation used in the remainder of this paper. As can be seen from Fig. 1, the onset of convection takes place at a higher Rayleigh number in the mixture than in a homogeneous fluid. The bifurcation is characterized by the values of the onset Rayleigh number r_{co} and the saddle node r_s. As the Rayleigh number is increased, the nature of the convection asymptotically approaches that in a pure fluid and becomes stationary at a Rayleigh number denoted as r^*.

It is convenient to introduce two new dimensionless parameters to describe convection in a mixture, the separation ratio ψ and the Lewis number $\mathcal{L}$:

$$\psi = -c(1-c)S_t \frac{\beta}{\alpha}, \qquad (4)$$

$$\mathcal{L} = \frac{D_c}{\kappa}, \qquad (5)$$

where $\beta = \rho^{-1}(\partial \rho / \partial c)$ is the solutal expansion coefficient. For $\psi < 0$, the Soret effect tends to stabilize the fluid layer against convection. The quantity ψ is a measure of the driving of convection due to Soret-induced concentration differences relative to that due to thermal expansion. The bifurcation diagram in Fig. 1 corresponds to $\psi < -\mathcal{L}$. For the mixture studied here, of 8% ethanol in water at a mean temperature of 25 °C, $\psi = -0.24$ [28]. The critical Rayleigh numbers in the largest circular container studied here are $r_{co} = 1.4$ and $r_s = 1.23$ [20]. The Lewis number $\mathcal{L} \simeq 0.01$, indicating the very slow time scale for the diffusion of concentration relative to that for heat, resulting in relatively long time scales for the dynamics.
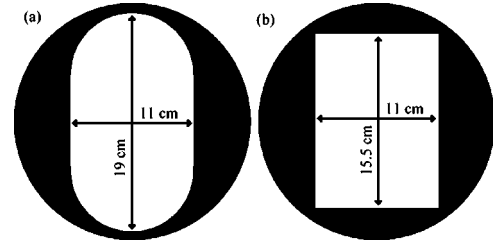

FIG. 2. Boundary shapes used in the present work. (a) Stadium-shaped cell, with a radius of curvature of the rounded ends of 5.5 cm and straight sections of length 8 cm; (b) rectangular cell of dimensions 11 x 15.5 cm^2. In addition, two circular cells were studied, having radii of 11 cm and 5.5 cm (see the text). The size of the larger circular cell is illustrated by the dark borders above. The height of all cells was 0.4 cm.

III. EXPERIMENT AND ANALYSIS TECHNIQUES

A. Apparatus

The experimental setup is similar to that described in detail in Ref. [20]. Convection is initiated by applying a temperature difference to the layer of the fluid mixture. The top-plate temperature is controlled by a flow bath. A film heater on the bottom plate is connected to a feedback loop that controls the temperature difference using the measured top- and bottom-plate temperatures as inputs. Using this arrangement, a temperature stability of less than 1 mK can be achieved over days, while the temperature difference is uniform over the whole cell to better than 3 mK. Patterns are visualized using a white-light shadowgraph and recorded using a charge-coupled device camera, computer controlled via a general purpose interface bus (GPIB).

In the experiments described here the height of the convection cell was fixed to 4 mm by a set of precision-ground glass spacers. Four cells with three different shapes were studied in order to elucidate the differences in the dynamics induced by the boundary geometry: two circular cells, a rectangular cell, and a stadium-shaped cell. To make contact with previous experiments, a circular cell with a radius of 11.0 cm and thus an aspect ratio ($\Gamma = R/h$) of 26 was used; this is the size of the cell used in Refs. [20–22]. The other shapes were obtained by placing a Teflon insert inside this cell. These inserts had the rectangular and stadium shapes cut out as shown in Fig. 2. The stadium-shaped insert was used to bridge the extreme cases of the circular and rectangular shapes. In order to check for a possible dependence of the patterns and their dynamics on cell size, a second circular cell was studied, with a radius of 5.5 cm (i.e., $\Gamma = 13$), corresponding to that of the curved parts of the stadium-shaped cell.

B. Analysis techniques

In discussions of pattern formation, it is customary to introduce an order parameter to describe the breaking of spatial symmetry leading to the pattern in question. In the case of traveling-wave convection, the oscillatory nature of the instability is accounted for by the assumption that the order parameter $A(\mathbf{x}, t)$ is complex. Thus the experimentally deter-

mined shadowgraph intensity, corrected for inhomogeneities in contrast by subtracting and dividing by an image in the quiescent state, is assumed to be the real part of a complex order parameter $A(\mathbf{x},t)$

$$I(\mathbf{x},t)=\mathrm{Re}[A(\mathbf{x},t)]=\|A(\mathbf{x},t)\|\cos[\phi(\mathbf{x},t)], \quad (6)$$

where $\phi(\mathbf{x},t)$ is the phase, and $\|A(\mathbf{x},t)\|$ is the amplitude of the order parameter. Since the amplitude is found to vary slowly in space and time, it is the spatial and temporal dependence of the phase that determines the wave vector and frequency of the pattern with

$$\partial_t\phi(\mathbf{x},t)=\omega(\mathbf{x},t), \quad (7)$$

$$\boldsymbol{\nabla}\phi(\mathbf{x},t)=\mathbf{k}(\mathbf{x},t). \quad (8)$$

In order to determine the phase and amplitude of the order parameter, we apply an algorithm similar to that employed by Egolf *et al.* [29] to determine the wave number in stationary patterns in a pure fluid. The key assumption in this analysis is that, away from defects in the pattern, the time dependence of the shadowgraph intensity is well approximated by a harmonic oscillator, and the phase of the order parameter varies much faster than its amplitude or frequency. In this case, the frequency is well approximated by

$$\omega^2(\mathbf{x},t)=-\frac{\partial_t^2 I(\mathbf{x},t)}{I(\mathbf{x},t)}. \quad (9)$$

This assumption is found to be valid for the experimental patterns studied here, after sufficient filtering to remove nonlinearities in the response of the shadowgraph. The phase of the order parameter is obtained using the measured frequency and the harmonic assumption as

$$\phi(\mathbf{x},t)=\tan^{-1}\left(\frac{\partial_t I(\mathbf{x},t)}{\omega(\mathbf{x},t)I(\mathbf{x},t)}\right), \quad (10)$$

and the amplitude of the order parameter is given by

$$\|A(\mathbf{x},t)\|=\left[I^2(\mathbf{x},t)+\left(\frac{\partial_t I(\mathbf{x},t)}{\omega(\mathbf{x},t)}\right)^2\right]^{1/2}. \quad (11)$$

Other properties of the pattern, such as the wave number $|\mathbf{k}(\mathbf{x},t)|$, the wave-vector direction $\mathbf{n}(\mathbf{x},t)=\mathbf{k}(\mathbf{x},t)/k(\mathbf{x},t)$, and the curvature $\boldsymbol{\nabla}\cdot\mathbf{n}(\mathbf{x},t)$, can then easily be determined from the phase.

Shown in Fig. 3 is an example of a demodulated shadowgraph image described above, for a traveling-wave state in the stadium-shaped cell. The raw shadowgraph image is shown together with the phase, amplitude, frequency, wave number, and wave propagation direction determined from the wave vector. As can be seen from the figure, most of the information about the pattern is contained in the phase field, and this is true for all the experiments conducted to date, irrespective of the particular shape of the cell boundary. The importance of the phase field was recognized in previous studies in a circular cell using a different demodulation al-
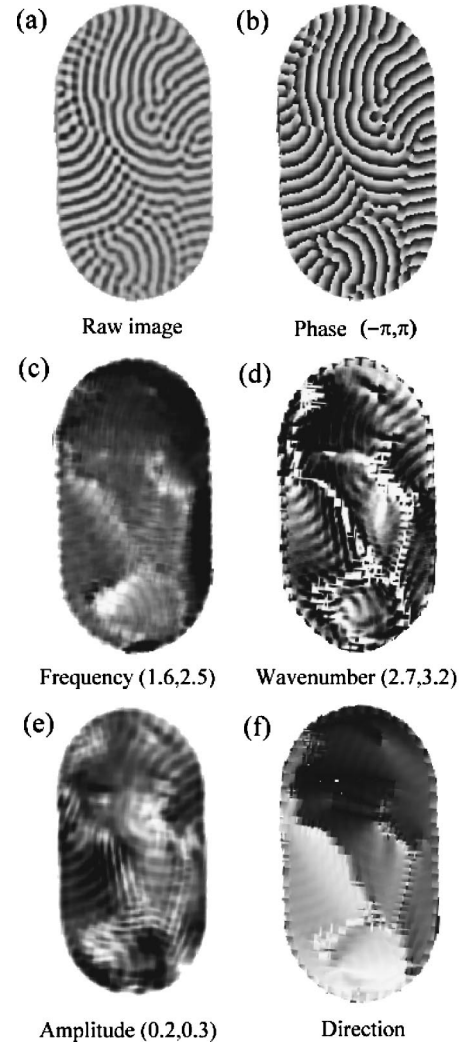

FIG. 3. An analysis of a shadowgraph image for a pattern in the stadium cell using the algorithm described in the text. The image was recorded at a Rayleigh number of $r=1.4$, after a long transient period. The scales are indicated in brackets (white,black). (a) Raw shadowgraph image, corrected for inhomogeneities in the shadowgraph intensity by subtracting and dividing by an image in the quiescent state; (b) the phase. In (c) the frequency ω is shown, normalized by τ^{-1}. The wave number, normalized by h^{-1}, is shown in (d). Finally, (e) and (f) show the amplitude of the order parameter and the direction of the wave vector, respectively.

gorithm [20], demonstrating that this basic result is independent of the details of the demodulation algorithm.

Previous discussions of the dynamics of traveling-wave convection have centered on the location and dynamics of topological defects in the phase field [21,22]. These studies were carried out in a circular container, where the patterns organized into a state with a small number of domains of locally parallel traveling waves separated by lines of topological defects. It was found [22,30] that the dynamics of the patterns could be reduced to a description in terms of phase defects. As discussed below, this is also found to be the case in the other cell shapes studied here. Hence we will analyze the patterns by identifying and tracking the topological defects in the phase field.
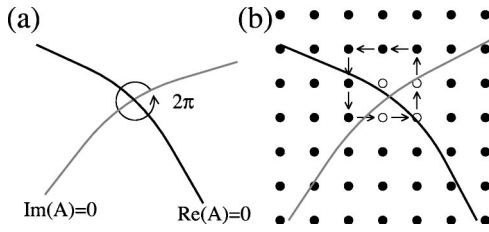
FIG. 4. (a) Schematic diagram of a topological defect in the phase field. (b) A similar schematic corresponding to the discrete case. Arrows indicate the path of integration around the pixel closest to the actual phase defect.

A topological defect in the phase is a singularity in the field at which the phase is undefined. This point is the crossing of zeros of the real and imaginary parts of the order parameter (see Fig. 4). However, due to the discretized nature of the experimentally determined phase fields, this definition is an unsuitable basis for a practical algorithm for calculation [22]. Alternatively, a contour integral around any point in the phase field gives a vanishing value except when the contour contains a topological defect, in which case,

$$\oint \phi d\theta = c 2\pi, \tag{12}$$

where c is the topological charge of the defect, which indicates the direction of the phase change around the contour of integration. In this paper $c > 0$ (< 0) corresponds to phase increasing in the counterclockwise (clockwise) direction. The integration of Eq. (12) can readily be discretized, and so it was used to determine the locations of topological defects by integrating the experimentally determined phase field along a loop around every camera pixel. An example of the results of this procedure is shown in Fig. 5, where the phase field of Fig. 3 is shown together with the corresponding defect map. In the following, we will focus on the dynamics and statistics of these defects and their relation to the physical patterns observed in the shadowgraph images.
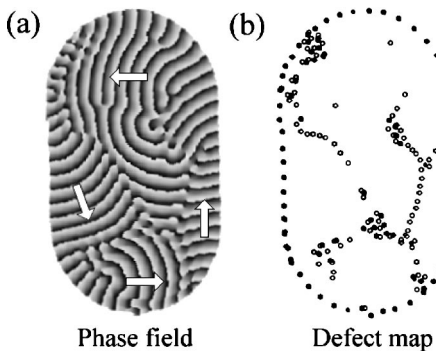

Phase field   **Defect map**

FIG. 5. The phase field determined from the shadowgraph image of Fig. 3(a), together with the map of topological defects. The defects were determined by calculating a contour integral around each pixel in the image (see text). The full circles correspond to defects of positive topological charge, and open circles are defects of negative charge.
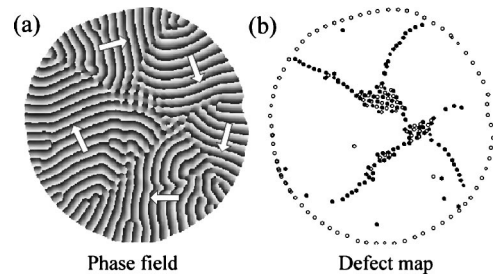

Phase field   **Defect map**

FIG. 6. The phase field and defect map in a circular cell (see also Ref. [21]) at $r = 1.4$. Departures from a circular boundary visible in the figure are due to obstructions in the optical path of the shadowgraph. The pattern rotates as a whole (in the clockwise direction), and so all of the defects at the boundary have the same (negative) charge. In the interior of the cell, the boundaries between the domains consist of lines of defects of the opposite charge (in order to conserve topological charge). (See text for details.)

In the remainder of this paper, time and distance are given in units of the thermal diffusion time ($\tau = h^2/\kappa = 124$ s) and the height of the cell ($h = 4$ mm), respectively.

IV. RESULTS AND DISCUSSION

We first present a brief summary of previous findings for the dynamics of traveling-wave convection in a circular container [21,22]. This discussion will focus mainly on the description of the dynamics in terms of topological defects in the phase field. In addition, we present recent data obtained in a smaller circular cell in order to study the effects of cell size on the pattern dynamics. This discussion will introduce many aspects of the phase defect description that are important in an understanding of the patterns and dynamics in the other container shapes studied.

Figure 6 shows the phase field and defect map for a traveling-wave pattern in a circular cell ($\Gamma = 26$) using the demodulation algorithm and defect identification techniques described above, after an initial period of self-organization. The most obvious feature is that all the phase defects on the boundary have the same charge (indicating that the rolls are traveling in the same angular direction along the edge of the cell). Four large domains of locally parallel traveling waves make up the bulk of the pattern. In the center of the cell, where the domains overlap, a region of cross-roll instability is observed. Apart from a small number of isolated dislocations, the domains consist of traveling waves of nearly constant wave number and frequency. In addition, lines of defects divide the different domains, some of which can also be identified with line sinks of traveling waves. Furthermore, the magnitudes of the phase velocity (but not the directions) in the different domains are very similar. The difference in the direction of the phase velocity is given by $\theta \simeq 2\pi/p$, where p is the number of domains. In the case shown, $p = 4$ so the traveling waves in the different domains propagate approximately at right angles.

The fact that the traveling waves in all the domains propagate clockwise with respect to the boundary leads to the impression that the pattern rotates as a whole (where the pattern rotation is about two times slower than the wave rotation).
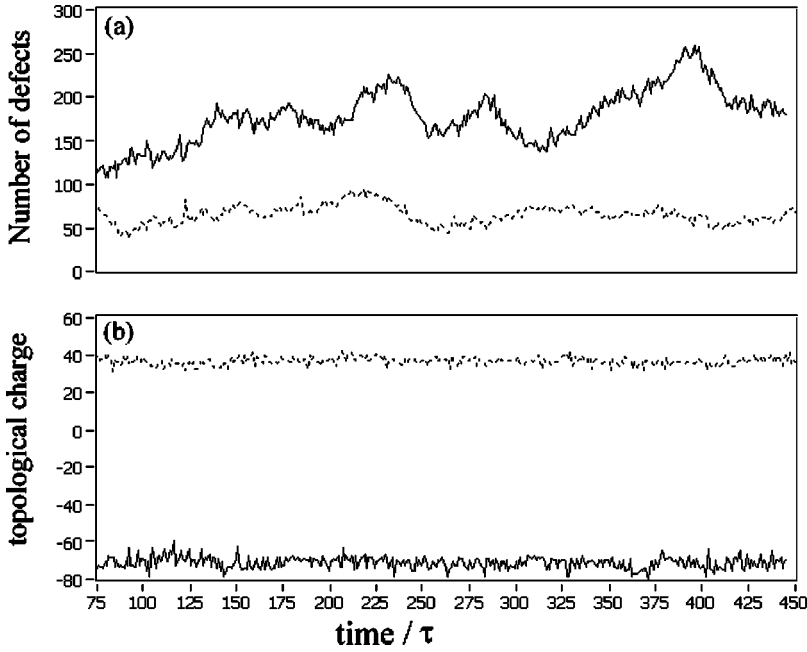
FIG. 7. Time evolution of the topological charge in the phase field and the number of defects in the large (solid) and small (dashed) aspect ratio circular containers, illustrating the dynamics of mature patterns in stable, globally rotating states. The net topological charge is constant and determined by the number of rolls around the circumference of the container. The total number of defects is larger than the net charge, reflecting the presence of cross-roll patches in the patterns. The similarity between the dynamics in the large and small aspect ratio containers shows that the dynamics of the patterns does not depend strongly on the size of the cell.

Since the sidewalls are thermally insulating, the rolls are oriented perpendicular to the boundary. Thus defects in the phase occur naturally at the boundary, with the sign of the defect charge indicting the direction of motion of the rolls. Due to the conservation of topological charge, this arrangement of rolls constrains the total charge within the pattern to be equal to that along the boundary [22]. This, in turn, leads to a total net topological charge in the interior of the container of $\mathcal{C} \simeq \pi \Gamma \simeq 74$; because every roll ends in a defect at the boundary, and the wave number is well approximated by $k = \pi$. Note that the total charge must be an even number, because rolls are created only in pairs.

From these considerations, it can be seen that, for a stably rotating pattern, the dynamics of the phase defects has to be relatively simple. The net charge $\mathcal{C}$ of the phase field must be constant in time and given by the roll wave number and the circumference of the boundary. The situation for the total number of defects is less simple. The intersections of domain boundaries within the cell frequently trigger regions of cross-roll instability which, in the phase defect picture, correspond to ordered lattices of positive and negative defects. The creation and destruction of cross-roll patches within the cell can lead to sizable fluctuations in the number of defects. However, in order to have a stable globally rotating state, the extent of such cross-roll patches is limited, and this leads to a limit in the fluctuations in the number of defects. The total number of defects $\mathcal{N}$ is approximately the total charge and the number of defects in the central cross-roll patch $\mathcal{N} = \mathcal{C} + \mathcal{N}_{CR}$. In the circular cell, $\langle \mathcal{N}_{CR} \rangle \simeq \mathcal{C}$, consistent with a small region in the center consisting of cross rolls. Assuming that the creation of cross rolls is a random process, a Poissonian distribution is expected, which would indicate that $\sqrt{\langle \Delta \mathcal{N}_{CR}^2 \rangle} \simeq \langle \mathcal{N}_{CR} \rangle \simeq \mathcal{C}$. This estimate is consistent with the data in Fig. 7, which shows the time evolution of both the total number of defects $\mathcal{N}$ and the topological charge $\mathcal{C}$, in both the large and the small aspect ratio circular containers. In both cases, the mature states of the patterns rotate glo-

bally, as illustrated by the constant topological charge. Furthermore, the patterns are well ordered as illustrated by the relatively constant total number of defects as a function of time (Fig. 7). In addition, the figure shows that all the major features of the dynamics scale with the system size. The different signs of the topological charge in the two cases indicate our general observation that global rotation is equally probable in both directions. Over many runs, we found an approximately equal distribution of directions.

We now refine the description of the dynamics in the circular container in terms of the motion of the phase defects in order to set the stage for a discussion of the dynamics in
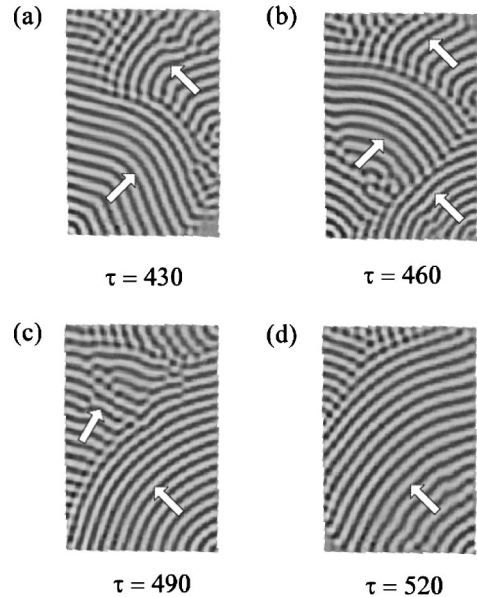

FIG. 8. Time evolution of the convection pattern in the rectangular cell, during the creation of a new traveling-wave source in the lower right corner (at $r = 1.37$). The new source evolves to dominate the entire pattern within $\sim 100\tau$ (see text for details).
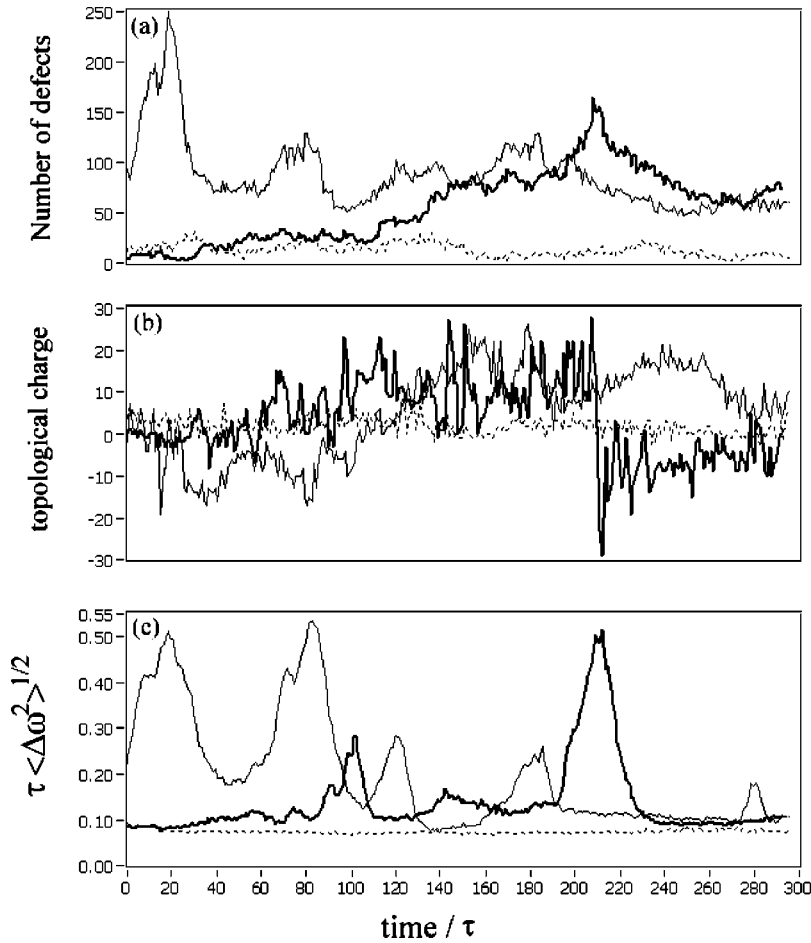
FIG. 9. Time evolution of the topological charge and the number of defects in the rectangular container. Dashed line, $r=1.39$, just above r_{co}; the pattern is very robust and dominated by a single source in one of the corners. Thick line, $r=1.37$; and thin line, $r=1.36$. In these cases, the (corner) location of the dominating source changes with time, and unsteady dynamics is observed. Also shown in the figure is the width of the frequency distribution averaged over the cell. When new sources appear, the pattern is strongly perturbed.

other boundary shapes. One of the dominant features in the patterns (cf. Fig. 6) is the lines of defects that form the boundaries between domains of traveling waves. Where these ''domain boundaries'' meet the cell boundary, the ''source'' of one domain of traveling waves coincides with a ''sink'' of the other. In terms of phase defects, a source of traveling waves consists of a location of pair production of defects of opposite charges. A sink in this respect can be treated as a point at which a positive and a negative defect annihilate. However, there is an asymmetry between sources and sinks in that line sources are observed, while sinks occur only as points. It is the fact that these domain boundaries meet the cell boundary that allows for the constant creation and annihilation of defect pairs at these points and the charge separation observed inside the cell and around the boundary. This will become important in the other cell geometries, where sources of traveling waves can appear on the boundary spatially separated from sinks. Furthermore, the cross-roll patches in the center of the cell are locations of pair creation and annihilation, which in some circumstances can spawn a new domain of traveling waves and thus also act as a source. Thus the appearance of sources of traveling waves, whether at the boundary or inside the cell, can deeply affect the statistics of the phase defects. This will turn out to be important in the rectangular and stadium-shaped cells discussed below.

A. Rectangular cell

Over large regions of Rayleigh number ($r>r_{co}$) the dynamics of the patterns in the rectangular cell are simpler than those observed in a circular container. Typically, sources of traveling waves form in the high-curvature regions in the corners of the rectangular cell, and these sources generate one dominant domain that fills the entire cell, resulting in a relatively uniform pattern. A pattern similar to this can be seen in Fig. 8(d), where a raw shadowgraph image at $r=1.37$ is shown. The fact that there is one dominant domain means that there is only one source and one corresponding sink of traveling waves in the pattern. This source is spatially fixed in one of the corners, while the sink is located in the opposing corner. Hence the net topological charge in the rectangular cell is typically stable and close to zero, since the defects are created in pairs at the source. There is only a very small number of defects in the interior of the cell, since there are no competing domains leading to cross-roll patches, and pair-created defects are annihilated in the sink. This can be seen by the dashed curve of Fig. 9, where the temporal evolutions of the topological charge and the number of defects are shown. The homogeneity of other parameters is illustrated by the width of the frequency distribution ($\sqrt{\langle \Delta \omega^2 \rangle}$) across the whole cell. In such a state, isolated occurrences of pair creation (and annihilation) of defects are observed routinely within a homogeneous domain of traveling waves. In
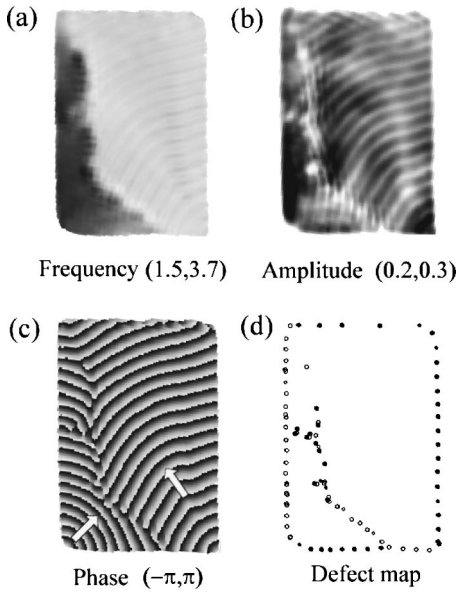
FIG. 10. Pattern in the rectangular cell during the creation of a new source in the lower left corner. (a) The frequency field, showing a large frequency difference between the competing domains. The frequency of the new source is close to the Hopf frequency, whereas the established domain is at the stable finite-amplitude traveling-wave frequency. Thus, there are different phase velocities in the two domains, and the new source invades the cell (see the text and Fig. 8). (b) The amplitude of convection, which is reasonably homogeneous across the two domains. Inspection of the phase field (c) shows that the wave number is different in the two domains. Finally, (d) shows the corresponding defect map with defects making up the boundary between the two domains.

the future, this situation may be useful in studying the conditions under which traveling waves are unstable to the production of isolated defects.

At smaller Rayleigh numbers, $r_s < r < r_{co}$, the dynamics is less steady. While sources of traveling waves are still localized in corners of the container, a single source in one corner no longer dominates the pattern (see Fig. 8). The effective Rayleigh number changes there, most probably due to the asymmetric proximity to a boundary in the lateral directions at different points close to the corners of the cell [18]. This may occur via an inhomogeneous mixing or macroscopic flows, leading to variations in the separation ratio at these locations. Transient regions of convection appear in these corners having very different frequencies of oscillation [23] as compared with the rest of the pattern. An example of this is illustrated in Fig. 10. When a new source appears, the frequency of the new domain is very close to the Hopf frequency, observed at the onset of convection. Thus the phase velocity ($v = \omega/k$) in these domains is much larger than that in the rest of the cell. Consequently, the traveling-wave domain belonging to the newly formed source spreads over much of the cell, while its frequency decreases slowly, evolving to the frequency of the stable traveling-wave branch. At this point the domains present in the cell have comparable phase velocities and subsequently coexist. In many cases, however, the spreading of the new source is fast enough to eliminate any other domain, at which point the

cycle can begin again (i.e., with an effectively reduced Rayleigh number in another corner). Consistent with this is the fact that the duration of the observed transients (see Fig. 9) corresponds to the time it takes for the phase to propagate across the whole cell. This process is illustrated in the time evolution shown in Fig. 8. Unfortunately, due to the very long time scales in this system, collecting enough statistics for a proper dynamical systems analysis of this switching phenomenon and reconstructing its attractor is impractical.

In Fig. 9 the defect statistics for two runs at lower Rayleigh numbers ($r = 1.37$ and $r = 1.36$) are also shown. The appearance of new sources can clearly be seen in the time dependence of the width of the frequency distribution. At times when new sources appear, the frequency width increases significantly due to the high frequencies introduced via the new source. Following the transient associated with such a switch in the dominant source, the frequency width returns to its previous smaller and constant value.

As was the case in the circular cell, the dynamics can be described in terms of the statistics of the phase defects. This is illustrated in Fig. 9. At high Rayleigh number, the net topological charge is constant and zero, and the number of defects in the cell is small and constant. There is a single, stable dominating source on the boundary, consistent with the net topological charge. The absence of cross-roll patches is indicated by the (small) total number of defects. The fact that stable sources can be located in the corners is most probably due to the very high curvature of the boundary in corners, which is zero elsewhere. In the stadium-shaped cell, the situation is different. Stable, spatially localized sources are not observed. Unstable sources do, however, appear along the boundary.

Now we turn to the more active dynamics observed at lower Rayleigh number (e.g., at $r = 1.37$) in the rectangular cell. In Fig. 9, the topological charge is constant during periods in which the pattern is stable and dominated by a single source or coexisting sources. The value of the charge depends on the distribution of the sources along the boundary and the locations of domain walls. However, when new sources appear, there is a change in the topological charge on a comparatively short time scale, corresponding to that of the high frequency transients described above. In Fig. 9, this is most clearly seen in the $r = 1.37$ data (thick line) at $t \simeq 210\tau$, where the charge changes from $\mathcal{C} \simeq 20$ to $\mathcal{C} \simeq -10$. In this case, the change in topological charge is large because sources in corners opposite each other compete for dominance. In addition, the resulting counterpropagating waves create regions of instability and hence a large increase in the number of defects in cross-roll patches. However, during another change in the dominating source (e.g., $t \simeq 100\tau$), there is no significant increase in the total number of defects. There is, however, a pronounced change in the net topological charge, since neighboring corners are switching and frequently a single line of defects divides the resulting domains. Similarly, the dynamics of the run at $r = 1.36$ (thin line) is reflected in the time evolution of the defect statistics. The appearance of new sources can be inferred from changes in the net topological charge of the pattern and also increases in the width of the frequency distribution. New sources appear-
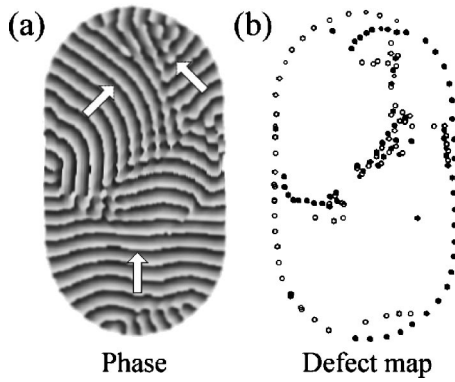
Phase　　　　Defect map

FIG. 11. Snapshot of the evolution of a pattern in the stadium-shaped cell at $r=1.37$. In contrast to the one shown in Fig. 5, this pattern does not rotate globally. This can also be seen in the distribution of topological charge around the boundary (see text).

ing in the corner opposite the dominant one are also marked by an increase in the total number of defects, due to the appearance of cross rolls at the boundary between the domains.

B. Stadium-shaped cell

The patterns in the stadium-shaped cell are more complicated than those in the rectangular cell. The boundary of the stadium cell is in some sense intermediate between those of the rectangular and the circular cells, and the patterns exhibit features reminiscent of both geometries. At high Rayleigh numbers $(r>r_{co})$, global rotation of the pattern does occur but does not appear to be stable. While small fluctuations typically do not destroy a globally rotating state and often damp out, large fluctuations or changes in the initial conditions can lead to dynamics which, even for very long times (e.g., up to 1 week), do not settle into a well defined state. This is illustrated in Fig. 11, where a snapshot of such a run

is shown together with the corresponding defect map. This figure can be compared to another run shown in Fig. 5 in which the system is in a globally rotating state. As was the case in the rectangular cell, global rotation of the pattern is absent in the presence of a source of traveling waves at the cell boundary. In contrast to the rectangular cell, however, the pattern in the stadium-shaped cell is not dominated by a single domain. Furthermore, a source at the boundary is typically not stationary in the stadium cell as it is in the rectangular cell, but moves along the curved parts of the boundary. This is plausible since the curvature is constant along this part of the cell, indicating a kind of symmetry between points there.

As was the case in the circular cell, the globally rotating states that are observed in the stadium cell can be described using the time evolution of the total number of defects in the pattern and the net topological charge. Again the charge inside the pattern matches that along the boundary and is constant in time. Furthermore, the value of the topological charge reflects the length of the circumference of the cell (i.e., the number of defects is equal to the circumference in units of the cell height). This is illustrated in Fig. 12, where the thin line shows a globally rotating state in the oval cell at $r=1.4$. This state was obtained by increasing the Rayleigh number from below onset to a value where the pattern is stationary. In this case, the pattern can be prepared with only a small number of defects. Then the Rayleigh number was decreased slowly to the traveling-wave regime, at which point the pattern begins to rotate. Once this state was obtained, the Rayleigh number was further decreased toward the saddle node.

In a state of global rotation, the total number of defects in the cell shows similar statistical properties to that in the circular cell, with $\sqrt{\langle\Delta\mathcal{N}_{CR}^{2}\rangle}\simeq\langle\mathcal{N}_{CR}\rangle\simeq\mathcal{C}$, where $\mathcal{C}\simeq56$ corresponding to the length of the boundary of the cell. As the Rayleigh number is decreased, small fluctuations can lead to
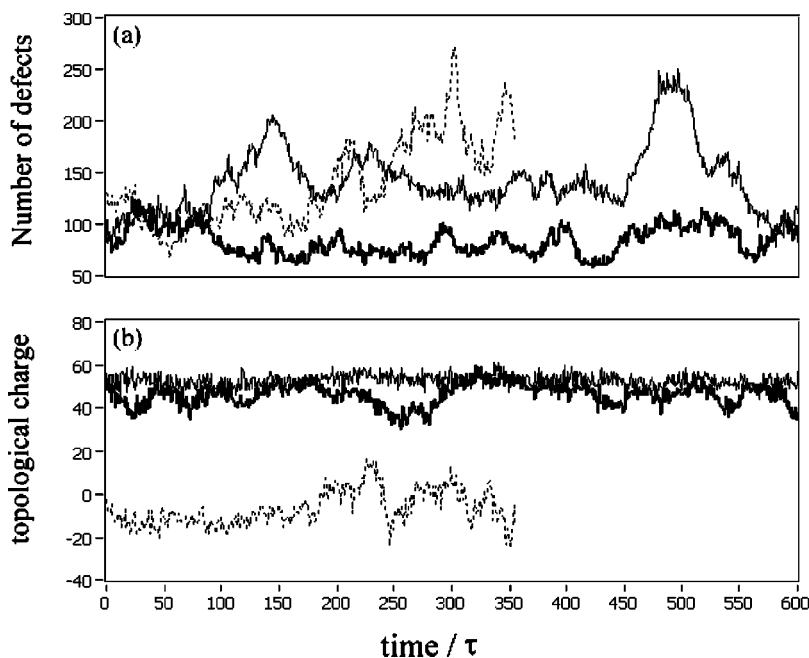

FIG. 12. Temporal evolution of the number of defects in the pattern and the topological charge in the stadium-shaped cell. The thin line shows a run at $r=1.4$. The same pattern was then taken at a lower Rayleigh number, $r=1.37$, as shown by the thick line. A run with another initial condition, but also at $r=1.37$, is shown by the dashed curve. Whereas the pattern at $r=1.4$ rotates globally, the situation is more complicated at the other two Rayleigh numbers.

departures from the rotating state, which in the stadium cell is less stable than in a circular container. Given a set of initial conditions leading to global rotation, however, such fluctuations are typically damped out. Small fluctuations are more common at lower Rayleigh numbers, and thus in this regime the pattern does not achieve a *stable* rotating state. This can be seen in the thick line in Fig. 12, which shows the time evolution of the total number of defects and the topological charge for a pattern at $r=1.37$ (i.e., a state reached by slowly reducing the Rayleigh number after the system is in a state of stationary convection). Earlier stages of this run gave rise to the dynamics shown by the thin line in Fig. 12 (i.e., a globally rotating state). At $r=1.37$ global rotation is not stable, but the pattern remains close to a state characterized by a constant net topological charge, the magnitude of which is still set by the length of the boundary. Figure 12 also shows a marked difference in the total number of defects between this state and the pattern at high Rayleigh number. Sources of traveling waves now exist along the boundary, and so the pattern is dominated by a smaller number of domains leading to a reduction in the total number of defects inside the cell. It is only when sources appear within the cell that a significant change in the number of defects is observed, which may, in turn, lead to the development of domain boundaries, and hence to a change in the global dynamics of the pattern. This is a mechanism by which, for instance, global rotation can be reachieved for short periods of time (e.g., around $t=300\tau$ in the thick line in Fig. 12).

Such changes can also be seen in the dashed curve of Fig. 12, which presents another run at $r=1.37$ with different initial conditions, far away from a rotating state. At $t \lesssim 50\tau$, a source inside the cell disappears, leading to a reduction in the number of defects. The appearance of sources of traveling waves along the boundary is again illustrated well by the changes in the topological charge of the pattern (e.g., at $t \simeq 180\tau$, 250τ, and 330τ in the dashed curve). In contrast to the sources in the rectangular cell, however, those in the oval cell may move along the boundary. Motion of these sources with respect to the sinks leads to gradual changes in the topological charge (e.g., Fig. 12, dashed curve, $100\tau < t < 180\tau$).

The correlation between changes in the topological charge and the number of defects is less pronounced in the stadium-shaped cell than in the rectangular cell. Increases in the number of defects in the stadium cell are due mainly to the appearance of sources of traveling waves within the cell. These sources subsequently influence only the global state of the pattern and hence the topological charge, as discussed above. However, the appearance of new sources along the boundary can still lead to an increase in the total number of defects, depending on the existence and location of a source within the cell beforehand. In case a source exists along the boundary beforehand, a competition between the domains corresponding to the sources will set in. This will lead to the creation of cross-roll patches and hence an increase in the number of defects in the pattern. In general, combining the information in the net topological charge with the number of defects allows a reasonably accurate description of the dynamics of the patterns, even in the complicated states occurring in the stadium cell.

C. Interaction of defects

Since most of the dynamics of the patterns can be described within the framework of topological defects in the phase field, it is interesting to further investigate their properties. As was done in Ref. [22], we have calculated the defect-defect correlation functions of both like and oppositely charged defects, which provide information about the mutual defect interaction potentials. The correlation functions are determined using the defect positions determined by the procedure described in Sec. III B:

$$C_{pp}(x,y) = \frac{1}{N_{pp}} \sum_{m \neq n} \delta_{(x_n - x_m),x} \delta_{(y_n - y_m),y} \delta_{c_n, c_m},$$

$$(13)$$

$$C_{np}(x,y) = \frac{1}{N_{pn}} \sum_{m \neq n} \delta_{(x_n - x_m),x} \delta_{(y_n - y_m),y} \delta_{c_n, -c_m},$$

where $\delta_{x,y}$ is the Kronecker delta function (which is 1 for $x=y$ and zero otherwise') and (x_n, y_n) and c_n are the Cartesian coordinates and the charge of the nth defect. The sum is over all defect pairs, and the correlation functions are normalized to the total number of defects. We average over many frames to obtain good statistics.

The information obtained from the correlation functions can be used to provide a crude interaction potential; however, by definition, it reflects only the probability of finding another defect (of like or opposite charge) at a specified distance away. Thus the structure of the correlation function is dominated by specific arrangements of defects in the pattern. In particular, cross-roll patches, with their well defined inter-defect distances, give rise to sharp peaks in the correlation functions, which can dominate their overall appearance. For this reason, we calculated a conditional defect-defect correlation function in which defects located in cross-roll patches were excluded. We used a criterion to decide whether a given defect is part of a cross-roll patch, as described in Ref. [22]. In particular, if the number of defects (of any charge) within a radius of $2h$ of a given defect exceeds 6, it is deemed to be part of a cross-roll patch and is excluded (in an ideal cross-roll patch, the number of such defects would be 12). Figure 13 shows the conditional correlation functions for the four different cells studied, where both C_{pp} and C_{np} have been azimuthally averaged. As can be seen from the figure, the general characteristics of the correlation functions are the same for all boundary shapes. Figure 13(a) shows the correlation function for like-sign defects. Peaks in correlation at h, $2h$, and $3h$ are still visible, in spite of the fact that defects in cross-roll patches have been excluded from the analysis. These peaks are due to the presence of the lines of like-sign defects between domains of traveling waves. In zipper boundaries, for example, the distance between defects is h, whereas in perpendicular boundaries it is $2h$. Ignoring the collective interactions that give rise to these effects, we see that there is a very strong repulsion of like-sign defects at
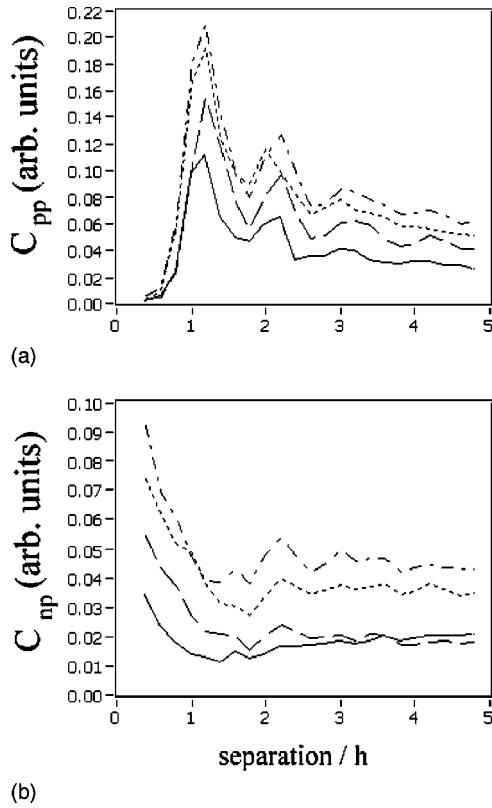
FIG. 13. The conditional correlation functions C_{pp} for like-sign defects (a); and C_{np} for opposite-sign defects (b). Full line, large aspect ratio circular container; long-dashed line, stadium-shaped cell; short-dashed line, rectangular cell; long-short-dashed line, small aspect ratio circular container. For defects of the same sign, the correlation function goes to zero for small values of separation of defects, indicating a repulsive interaction at short distances. For oppositely charged defects, the correlation function increases for small separation, indicating an attractive potential.
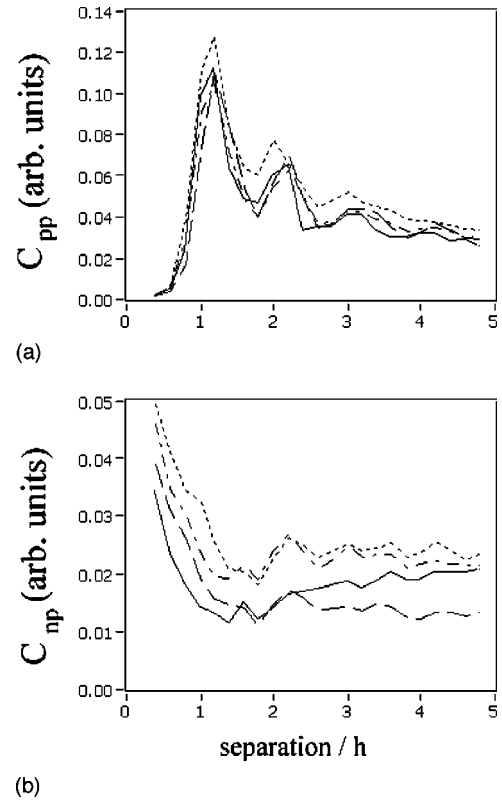

FIG. 14. Rescaled correlation functions for (a) like-sign defects C_{pp}, and (b) opposite-sign defects C_{np}. The data are the same as in Fig. 13, but scaled by multiplying by the square root of the lateral convection cell area. The same notations are used. For defects of the same sign, this rescaling works well. For oppositely charged defects, the scaling is not as good (see text for details).

short distances, as well as a small attractive force between defects at larger distances. Note also the increase in correlation with decreasing system size.

In Fig. 13(b), the correlation function for oppositely charged defects is shown. In contrast to the case for like-sign defects, the correlation function continues to increase at small distances. This indicates a short-range attraction of oppositely charged defects. The dip in C_{np} present at $\sim 1.5h$ indicates the existence of a small potential barrier in the interaction between defects. At shorter distances, the interaction is strongly attractive, and defects come together and annihilate. At larger distances the interaction is slightly repulsive.

In order to understand the dependence of C_{np} and C_{pp} on the size of the container indicated above, we have rescaled the correlation functions by the square root of the respective areas of the different convection cells. As can be seen in Fig. 14(a), this scaling works well for the correlations of like-sign defects. This is probably due to the fact that most of the defects of the same sign are arranged in lines corresponding to the domain boundaries. Thus in the normalization of the correlation functions [i.e., Eq. 13)], the number of pairs of defects contributing to C_{np} and C_{pp} at short distances is

overcounted. In contrast, the correlations between oppositely charged defects do not obey this scaling as precisely, as can be seen in Fig. 14(b). While the general trend of decreasing correlations with increasing system size is still observed in C_{np}, the lack of exact scaling may indicate a slight difference in the interactions of unlike-sign defects in different containers. Alternatively, the different total number and charge of defects in the various containers could result in a different statistical sampling of C_{np}.

V. CONCLUSIONS

We have presented a study of the dynamics of traveling-wave convection in large aspect ratio containers. It is found that there is a strong dependence of the global dynamics on the shape of the lateral boundary. In a circular container, the pattern evolves to a stable state, composed of several domains of locally parallel traveling waves, and exhibits global rotation, apparently irrespective of the size of the system. In contrast, the dynamics in a rectangular cell is dominated by a single domain of traveling waves originating in one corner of the cell. For Rayleigh numbers close to the saddle node, the dominance of a particular corner changes with time, and we speculate that this is due to a change in effective Rayleigh number close to the corners. This in turn is likely to be due to the close presence of two boundaries at these points that

can influence the properties of the instability [19,18]. Qualitatively similar behavior is observed in a stadium-shaped cell; however, due to the curvature in the boundary, the dynamics of the patterns in the stadium cell is somewhat different. Sources appearing at the boundary are not confined to specific locations but move continually. Depending on the value of the Rayleigh number and on the initial conditions, globally rotating states may be observed, but they are not stable at long times.

We have shown that these different dynamical behaviors can be described in terms of the dynamics of topological defects in the phase of the complex order parameter. A key insight gained from this picture is the fact that topological charge is conserved, which leads to a balance of defects at the boundary and within the cell. A rotating state is characterized by a constant net charge on the boundary, achieved by the presence of lines of defects located in domain boundaries in the interior of the cell. Sources of traveling waves can be identified as locations of pair creation of defects, and the time evolution of the number of defects and the topological charge can be used as a simplified description of the dynamics of the patterns. This general description of patterns in terms of phase defects still holds for the more complicated dynamics observed in the stadium-shaped cell.

Finally, we have investigated the *local* interactions between both like-sign and opposite-sign defects. The interactions are similar in all the cell shapes studied here. Oppositely charged defects exhibit an attractive interaction potential, but have a small potential barrier at distances of the order of the height of the fluid layer. In contrast, like-sign defects exhibit a short-range repulsive potential, which can be approximated by a hard-core potential, and a small attractive interaction at larger distances. These findings for the correlation functions are consistent with previous investigations in a circular cell [22] and indicate that the local interactions between defects do not vary with the shape of the container boundary. Thus there appear to be additional non-local and/or collective interactions that are responsible for the very different global dynamics of the patterns observed in the different cells.

ACKNOWLEDGMENTS

[1] M.C. Cross and P.C. Hohenberg, Rev. Mod. Phys. **65**, 851 (1993).

[2] R.W. Walden, P. Kolodner, A. Passner, and C.M. Surko, Phys. Rev. Lett. **55**, 496 (1985).

[3] P. Coullet, L. Gil, and F. Rocca, Opt. Commun. **73**, 403 (1989); K. Staliunas, Phys. Rev. A **48**, 1573 (1993); J. Lega, J.V. Moloney, and A.C. Newell, Phys. Rev. Lett. **73**, 2978 (1994).

[4] R.M. May, Nature (London) **261**, 459 (1974); P. Kareiva and U. Wennergren, *ibid.* **373**, 299 (1995).

[5] F. Pociot, B. Freisleben, P. Bak, and A.E. Karlsen, Diabetes **47**, 846 (1998).

[6] L. Glass and P. Hunter, Physica D **43**, 1 (1990); *Mathematical Approaches to Cardiac Arrythmias*, edited by J. Jalife special issue of Ann. N.Y. Acad. Sci. **591** (1990); A.L. Hodgkin and A.F. Huxley, J. Physiol. (London) **117**, 500 (1952).

[7] A.M. Turing, Philos. Trans. R. Soc. London, Ser. B **237**, 37 (1952).

[8] A.N. Zaikin and A.M. Zhabotinskii, Nature (London) **225**, 535 (1970); Q. Ouyang and H.L. Swinney, *ibid.* **352**, 610 (1991).

[9] S.M. Tobias, M.R.E. Proctor, and E. Knobloch, Astron. Astrophys. **318**, L35 (1997).

[10] J.J. Bonner, *The Cellular Slime Molds* (Princeton University Press, Princeton, NJ, 1967).

[11] H. Levine and W. Reynolds, Phys. Rev. Lett. **66**, 2400 (1991); E. Ben-Jacob, O. Shochet, A. Tenenbaum, I. Cohen, A. Czirok, and T. Vicsek, Nature (London) **368**, 46 (1994).

[12] R. Surdeanu, R.J. Wijngaarden, B. Dam, J. Rector, R. Griessen, C. Rossel, Z.F. Ren, and J.H. Wang, Phys. Rev. B **58**, 12 467 (1998).

[13] C.M. Aegerter, Phys. Rev. E **58**, 1438 (1998).

[14] S. Chandrasekar, *Hydrodynamic and Hydromagnetic Stability* (Clarendon Press, Oxford, 1961).

[15] R.M. Clever and F.H. Busse, Phys. Rev. E **57**, 4198 (1998).

[16] See, e.g., Ch. Jung, Ph.D. thesis, University of Saarbrücken, 1997.

[17] D. Roth, P. Büchel, M. Lücke, H.W. Müller, M. Kamps, and R. Schmitz, Physica D **97**, 253 (1996).

[18] S.M. Tobias, M.R.E. Proctor, and E. Knobloch, Physica D **113**, 43 (1998).

[19] M.C. Cross, Phys. Rev. Lett. **57**, 2935 (1986); , Phys. Rev. A **38**, 3593 (1988).

[20] A. LaPorta and C.M. Surko, Phys. Rev. E **53**, 5916 (1996).

[21] A. LaPorta and C.M. Surko, Phys. Rev. Lett. **77**, 2678 (1996).

[22] A. LaPorta and C.M. Surko, Phys. Rev. E **56**, 5351 (1997).

[23] St. Hollinger and M. Lücke, Phys. Rev. E **57**, 4238 (1998).

[24] P. Kolodner and H. Williams, in *Nonlinear Evolution of Spatio-Temporal Structures in Dissipative Continuous Systems*, edited by F.H. Busse and L. Kramer (Plenum, New York, 1990), pp. 73–91.

[25] P. Manneville, *Dissipative Structures and Weak Turbulence* (Academic, Boston, 1990).

[26] L.D. Landau and E.M. Lifshitz, *Fluid Mechanics*, Vol. 6 of *Course of Theoretical Physics* (Pergamon, Oxford, 1987).

[27] J.K. Platten and J.C. Legros, *Convection in Liquids* (Springer-Verlag, Berlin, 1984).

[28] P. Kolodner, H. Williams, and C. Moe, J. Chem. Phys. **88**, 6512 (1988).

[29] D.A. Egolf, I.V. Melnikov, and E. Bodenschatz, Phys. Rev. Lett. **80**, 3228 (1998).

[30] A. LaPorta and C.M. Surko, Physica D **139**, 177 (2000).